DEFECT SIZING WITH A 'WELDSCAN' PROBE USING AN EDDY-CURRENT MODEL

S. A. Jenkins[1] and John Hansen[2]
[1] Current Enterprise Ltd., Kent, UK; [2] Hocking NDT Ltd., St. Albans, UK

Abstract: In this paper we apply a well-established eddy-current model to a 'WeldScan' probe, a more complicated type of probe, in order to better understand its characteristics. After validating the model to new experimental results, the complex interaction of the fields with defects is explored. It is then shown, that under certain simplifying assumptions on defect orientation and topology that the eddy-current signals can be correlated to defect size and location. The eddy-current model is based on a volumetric integral approach using dyadic Green's functions and has been used extensively for over ten years. The 'WeldScan' probe has been in the field for over sixteen years and has two "tangent coils" which can be driven separately, or in tandem in absolute or differential modes. Due to the coils being 'on edge', the coupling of the probe with the work-piece is poorer than traditional coils; however, the coils orientations allow for better probe access and form characteristics. Another advantageous characteristic of this probe is the large, uniform field that is generated at 45° at the intersection of the coils. The uniform nature of this field allows for much easier correlation of probe signal to defect size and location. The incident field generated by the probe was modeled and used to drive the model. Experimental results were then used to validate the model with manufactured defects in aluminum. The model was then used to show that the probe's signals can be correlated to defect size and location, with some simple assumptions on defect orientation and overall shape.

Introduction: Traditional eddy-current probes have their driving coil, often called *pancake coils,* parallel to the surface being investigated. Small diameter coils achieve high resolution, but poor depth of penetration, while large diameter coils have good depth of penetration, but have poor resolution and also present packaging and deployment issues due to their large surface area. Another feature of pancake coils is their sensitivity to *lift-off*. Therefore, eddy-current probe design has always involved some sort of trade-off between resolution and depth of penetration. The *weld scan* probe was developed to overcome some of these problems. This probe uses two interwoven *tangential* coils.

Tangential coils are coils whose axes are parallel to the surface; the coil is 'on edge' as is shown in figure 1. The field induced in the work-piece is also shown in the Figure. The field is no longer axially symmetric and has some interesting characteristics, especially when both coils are driven, as shown in Figure 2. The maximum field strength occurs at the edges of the coil directly underneath the coil. The eddy currents flow parallel to the surface, just like the pancake coil.

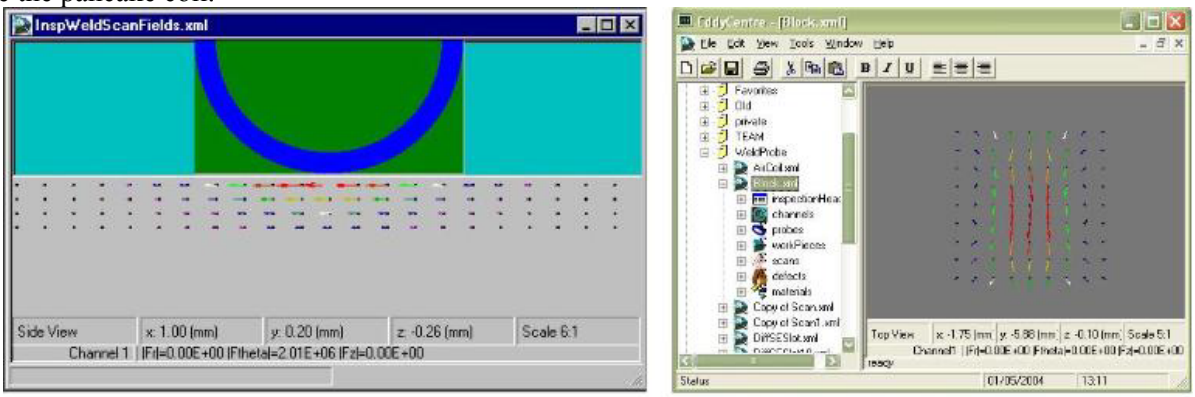

Figure 1 - Tangential coil and associated electric field inside an aluminum block

Eddy-Current Model: A general eddy current model[1] was used with the WeldScan probe. The model was developed using the method of moments, the derivation and description, however, is beyond the scope of this paper. The model involves dividing only the defect volume into regular volumetric cells and using a dyadic Green's function operator to define how these cells interact with each other for a given incident electric field, the forcing function of the model. For the results discussed in this paper, three defects were modeled: 0.1x20x2mm,

0.1x10x1mm and 0.1x5x0.5 deep semi-elliptical slots were modeled using 24x1x4 cells. The dyadic Green's function operator, A, is described as a 3*n* x 3*n* matrix, where *n* is the number of cells in the defect volume, i.e. 96. The unknowns in this model are the dipole densities at the center of each of the defect volumes.

The eddy current model used involves solving for the incident field, **y**, at the center of each defect cell for each probe position. Then we have the relationship that A**x** = **y**, where **x** is the vector of unknown dipole densities. We can solve this equation for **x** which yields, $\mathbf{x} = A^{-1}\mathbf{y}$. The change in the coil's impedance is, due to reciprocity, equal to the impedance of the eddy currents flowing in the defect volume which is, $\Delta z = c\mathbf{x}\cdot\mathbf{y}$, for a scalar *c*. The only difference in applying this model to pancake coils versus tangential coils is the in calculating the incident field vector **y**. The model interpolates the fields, like those shown in Figure 1, at the center of the defect volumetric cells. In order to model the WeldScan probe, it was only necessary to model the new forcing function, the incident field from this probe, at the center of each of the defect volumes.

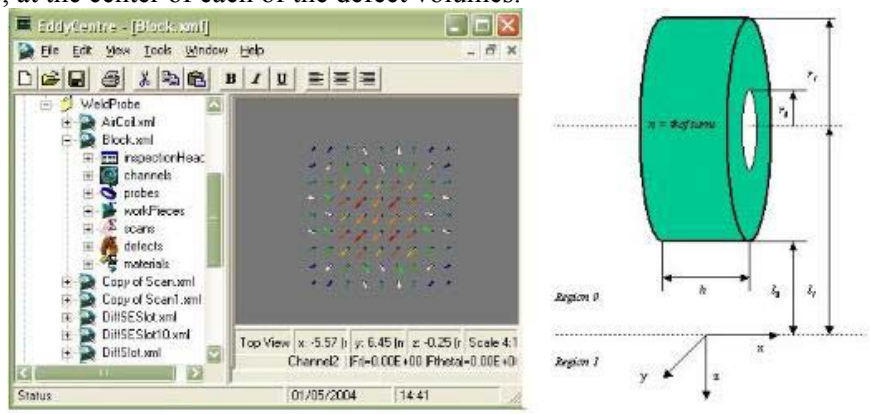

Figure 2 -Fields from 2 interwoven tangential coils and coil parameters

Although the source term **J(r)** is the same for pancake and tangent coils, it has a different orientation. Referring to Figure 2, we define the source current density[2]

$$\mathbf{J}(r', y', \theta') = \frac{\iota_0}{h(r_1 - r_0)}\hat{\theta}', \tag{1}$$

for $r_0 < r < r_1$ and $-h/2 < y < h/2$. The axis of the current loop is now parallel to the surface of the conductor and a distance $l_1 = l_0 + r_1$ from it. The general form of the vector potential can be written

$$\mathbf{A}_j(\mathbf{r}) = i\omega\mu_0 \nabla \times \hat{z}\Pi_j^{(e)} \tag{2}$$

where **A(r)** is the free-space vector potential and $\mathbf{A}_f(\mathbf{r}_i)$ is the free-space vector potential of the image term, assuming perfect reflection, and $\mathbf{r}_i = \mathbf{r} - 2z\mathbf{z}$ where *z* is the component of **r** in the **z** direction. In the absence of a conductor only the free-space term is non-zero.

These results can be used to construct dyadic Green's functions, $\check{\mathbf{G}}_j$, which can transform the current source **J** directly into the vector potential **A**. For planar isotropic stratified regions beneath the probe, i.e. *j>0,*

$$\mathbf{A}_j(\mathbf{r}) = i\omega\mu_0 \int \vec{\mathbf{G}}_j(\mathbf{r}, \mathbf{r}') \cdot \mathbf{J}(\mathbf{r}')d\mathbf{r}' \tag{3}$$

and for region *j=0*, the probe region,

$$\mathbf{A}_0(\mathbf{r}) - \mathbf{A}_f(\mathbf{r}) - \mathbf{A}_f(\mathbf{r}_i) = i\omega\mu_0 \int \vec{\mathbf{G}}_0(\mathbf{r}, \mathbf{r}') \cdot \mathbf{J}(\mathbf{r}')d\mathbf{r}', \tag{4}$$

where

$$\vec{\mathbf{G}}_j(\mathbf{r}, \mathbf{r}') = -\nabla_t^2 \Pi_j(\mathbf{r}, \mathbf{r}') \tag{5}$$

As in the case of pancake coils, we make use of a two-dimensional Fourier transformation, writing $\check{\mathbf{G}}$ as

$$\widetilde{G}_j(\mathbf{r}|\mathbf{r}') = \frac{1}{(2\pi)^2}\int_{-\infty}^{\infty}\int_{-\infty}^{\infty} g_j(u,v,z,z')e^{iu(x-x')+iv(y-y')}dudv \tag{6}$$

where $\alpha^2 = u^2 + v^2$ and $\alpha^2 = \alpha^2 - k_i^2$. We find on integration of equation (5)

$$\nabla_t \Pi_j^{(e)} = \frac{1}{(2\pi)^2}\int_{-\infty}^{\infty}\int_{-\infty}^{\infty}\frac{1}{2\alpha^2}\left[\Gamma_{j+1}e^{\alpha_j z-\alpha_0 z'} + \Upsilon_j e^{-\alpha_j z+\alpha_0 z'}\right]e^{iu(x-x')+iv(y-y')}dudv \tag{7}$$

where Γ and Y are the reflection and transmission coefficients for region *j*, respectively.

The reduced scalar potential W_j is given by

$$W_j(\mathbf{r}) = \int_{\Omega_j}\nabla_t\Pi_j^{(e)}\cdot\mathbf{J}(\mathbf{r}')d\mathbf{r}' \tag{8}$$

Integrating equation (8) over the source coordinates given by equation (1) we find

$$\begin{aligned}\mathbf{A}_j(\mathbf{r}) &= \int_{-\frac{h}{2}}^{\frac{h}{2}}\int_{r_0}^{r_1}\int_0^{2\pi}\int_{-\infty}^{\infty}\int_{-\infty}^{\infty}\frac{iv}{2\pi^2\alpha_0\alpha^2}\left[\Gamma_{j+1}e^{\alpha_j z-\alpha_0 z'} + \Upsilon_j e^{-\alpha_j z+\alpha_0 z'}\right]\\ &\cdot e^{iu(y-y')+iv(x-x')}\frac{\iota_0}{h(r_1-r_0)}\hat{\theta}'r'dudvd\theta'dr'dx'\end{aligned} \tag{9}$$

Substituting the relations

$$\begin{aligned}\hat{y}\cdot\hat{\theta}' &= \cos\theta \qquad \hat{x}\cdot\hat{\theta} = 0\\ z' &= l_1 + r'\cos\theta' \quad y' = r'\sin\theta',\end{aligned} \tag{10}$$

into equation (9) yields

$$\begin{aligned}\mathbf{A}_j(\mathbf{r}) &= \frac{i\iota_0}{2\pi^2 h(r_1-r_0)}\int_{-\frac{h}{2}}^{\frac{h}{2}}\int_{r_0}^{r_1}\int_0^{2\pi}\int_{-\infty}^{\infty}\int_{-\infty}^{\infty}\frac{v}{\alpha_0\alpha^2}\left[\Gamma_{j+1}e^{\alpha_j z-\alpha_0(l_1+r'\cos\theta')} + \Upsilon_j e^{-\alpha_j z+\alpha_0(l_1+r'\cos\theta')}\right]\\ &\cdot e^{iu(y-r'\sin\theta')+iv(x-x')}r'\cos\theta' dudvd\theta' dr'dx'\end{aligned} \tag{11}$$

Changing the order of integration and integrating with respect to *x′*, recognizing that

$$\int_{-\frac{h}{2}}^{\frac{h}{2}}e^{ivx'}dx' = \int_{-\frac{h}{2}}^{\frac{h}{2}}\cos vx' - \sin ivx \quad dx' = h\mathrm{sinc}\frac{vh}{2} \tag{12}$$

where sinc(*x*) = sin(*x*)/*x*, we have

$$\begin{aligned}\mathbf{A}_j(\mathbf{r}) &= \frac{i\iota_0}{2\pi^2(r_1-r_0)}\int_{-\infty}^{\infty}\int_{-\infty}^{\infty}\int_0^{2\pi}\int_{r_0}^{r_1}\Gamma_{j+1}\mathrm{sinc}(\frac{vh}{2})\frac{v}{\alpha_0\alpha^2}e^{ivx+iuy+\alpha_j z-\alpha_0 l_1}\\ &\cdot e^{-\alpha_0 r'\cos\theta'-iur'\sin\theta'}r'\cos\theta' d\theta' dr' dudv\\ &+ \frac{i\iota_0}{2\pi^2 h(r_1-r_0)}\int_{-\infty}^{\infty}\int_{-\infty}^{\infty}\int_0^{2\pi}\int_{r_0}^{r_1}\Upsilon_j\mathrm{sinc}(\frac{vh}{2})\frac{v}{\alpha_0\alpha^2}e^{ivx+iuy-\alpha_j z+\alpha_0 l_1}\\ &\cdot e^{\alpha_0 r'\cos\theta'-iur'\sin\theta'}r'\cos\theta' d\theta' dr' dudv\end{aligned} \tag{13}$$

Carrying out the integral with respect to α' using the Bessel function identity,

$$\int_0^{2\pi}e^{p\cos\theta'+iq\sin\theta'}\cos\theta' d\theta' = \frac{2\pi p}{\sqrt{p^2-q^2}}I_1(\sqrt{p^2-q^2}), \tag{14}$$

and assuming the quasi-static limit, which implies $\alpha_0 \approx \alpha$, yields

$$\mathbf{A}_j(\mathbf{r}) = \frac{i\iota_0}{\pi(r_1-r_0)}\int_{-\infty}^{\infty}\int_{-\infty}^{\infty}\int_{r_0}^{r_1}\frac{r'}{\alpha^2}I_1(r'v)\Gamma_{j+1}\mathrm{sinc}(\frac{vh}{2})e^{ivx+iuy+\alpha_j z-\alpha l_1}dr'dudv$$
$$- \frac{i\iota_0}{\pi h(r_1-r_0)}\int_{-\infty}^{\infty}\int_{-\infty}^{\infty}\int_{r_0}^{r_1}\frac{r'I_1(r'v)}{\alpha^2}\Upsilon_j\mathrm{sinc}(\frac{vh}{2})e^{ivx+iuy-\alpha_j z+\alpha l_1}dr'dudv \quad (15)$$

Integrating with respect to r' is handled by introducing the function $\Phi(s) = \int_0^1 \rho I_1(s\rho)d\rho$, therefore, equation (15) can be rewritten as

$$\mathbf{A}_j(\mathbf{r}) = \frac{i\iota_0}{\pi(r_1-r_0)}\int_{-\infty}^{\infty}\int_{-\infty}^{\infty}\frac{[r_1^2\Phi(r_1v)-r_0^2\Phi(r_0v)]}{\alpha^2}\mathrm{sinc}(\frac{vh}{2})e^{ivx+iuy}$$
$$\cdot\left[\Gamma_{j+1}e^{\alpha_j z-\alpha l_1}-\Upsilon_j e^{-\alpha_j z+\alpha l_1}\right]dudv \quad (16)$$

This is the expression that we desire and was used to generate the fields shown in Figure 1 and provides the forcing function in all the modeling results that follow.

Model Results: The eddy-current model was used to model six different defects:

- 0.1 x 5 x 0.5 mm, 0.1 x 10 x 1 mm and 0.1 x 20 x 2 mm rectangular notches
- 0.1 x 5 x 0.5 mm, 0.1 x 10 x 1 mm and 0.1 x 20 x 2 mm semi-elliptical notches.

The defects were modeled in aluminum at 100 kHz with a skin depth of approximately 5mm. The probe had two driving/receiving coils with inner and outer radius 4 and 4.75 mm, respectively, with a height of .75 mm. The coils are mounted tangentially, with each coil normal to the other. The probe can be used in *absolute mode*, where only one coil is used, which produces the fields shown in Figure 1, where the change in impedance in the coil is modeled. The probe can also be used in *differential mode*, where both coils are driven, which produces the fields shown in Figure 2, and the difference between the impedance changes of the coils is modeled.

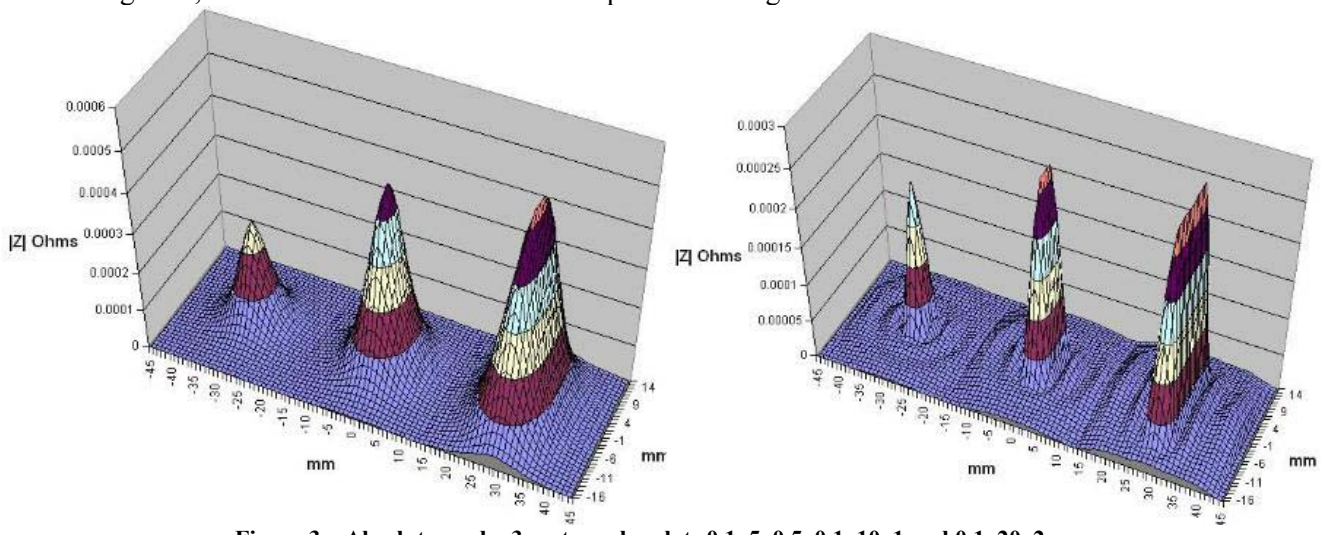

Figure 3 – Absolute mode: 3 rectangular slots 0.1x5x0.5, 0.1x10x1 and 0.1x20x2 mm

The results shown if Figure 3 were obtained by modeling the 3 rectangular slots in absolute mode, with a scanning resolution of 1 x 1 mm. The results on the left in the Figure were obtained with the driving coil normal to the defects, while the results on the right were obtained with the coil parallel to the defects. The plot with the coil normal to the defects is twice the scale as that with the coil parallel to the defects. When the coil is normal to the defects, the field, and therefore the eddy-currents, hit the side of the defect and cause a much larger impedance change in the driving coil. When the coil is parallel to the defect, the eddy-currents mostly flow uninterrupted past the defect. However, the parallel scan does have a much narrower focus, which would make defect sizing and location easier.

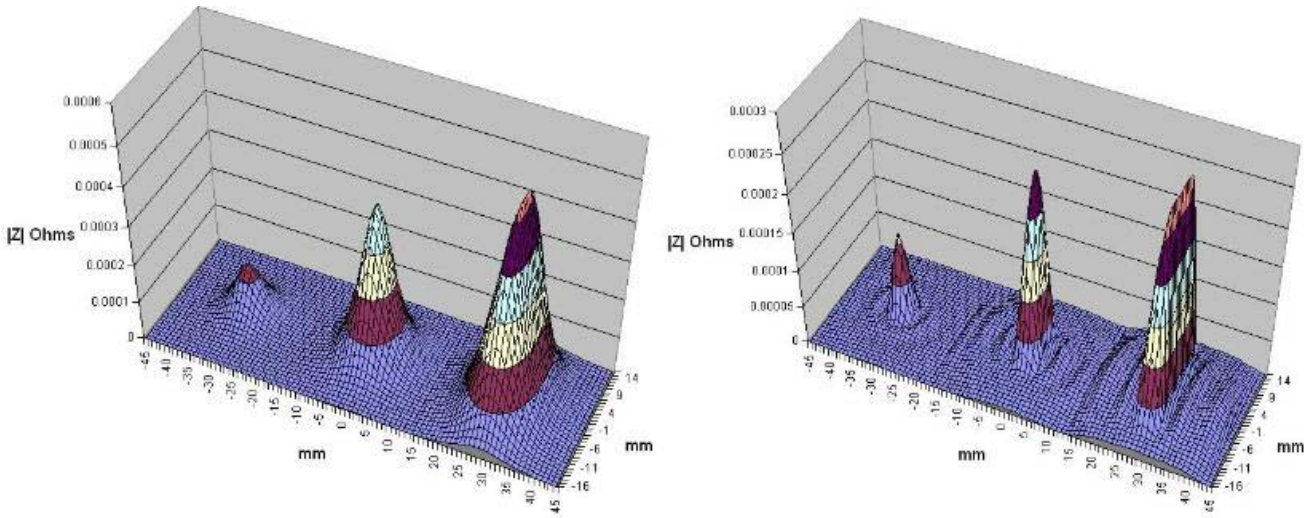

Figure 4 – Absolute mode: 3 semi-elliptical slots 0.1x5x0.5, 0.1x10x1 and 0.1x20x2 mm

The results shown in Figure 4 were obtained by modeling the 3 semi-elliptical slots in absolute mode, with the same 1 x 1 mm scanning resolution. Again the normal coil generates approximately twice the impedance change as the parallel coil and the parallel coil has a tighter focus. Comparing Figures 3 and 4 we see that for the shallower defects there is a much bigger change in the impedance signal due to the rounded shoulders of the notches, where the deeper notch, with a depth of approximately half a skin depth, is much harder to differentiate a difference in the signal.

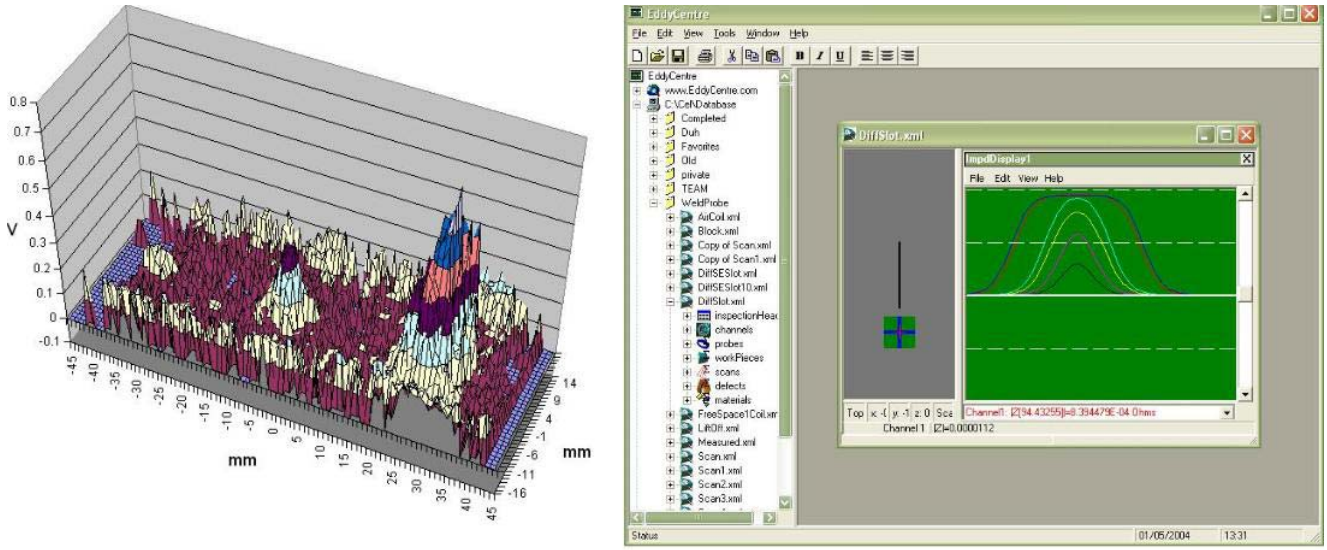

Figure 5 – Measured data in differential mode with 3 semi-elliptical slots and modeled central line scans over 6 defects

The left side of Figure 5 shows the results of an actual scan using the WeldScan probe in differential mode of 1 x 1 mm resolution over an aluminum block with 3 etched semi-elliptical slots of the same size as those modeled. All though the signal is noisy, the 3 defects can be clearly discerned. There is an edge effect signal running down both sides of the block as well. The 3 semi-elliptical slots were modeled, as well as the 3 rectangular slots were modeled in differential mode. The *signal profiles*, the signal generated from scanning down the centerline of the defects, are shown on the right of Figure 5. The smallest of each pair of signals represents the signal from the semi-elliptical slots. The profiles and magnitudes are in good agreement with the measured results.

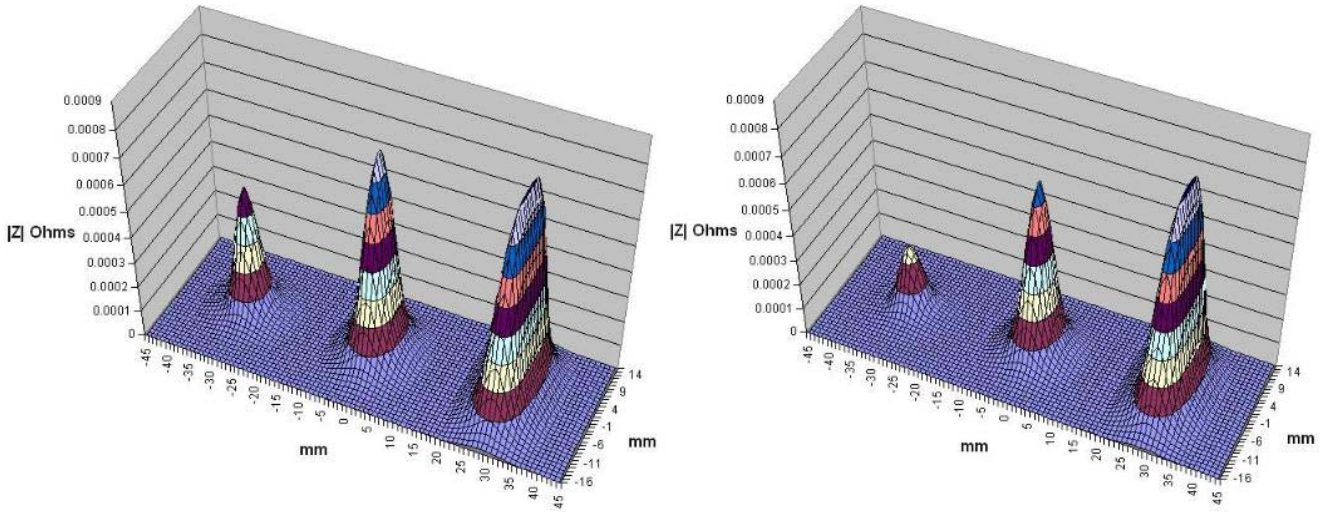

Figure 6 – Differential mode: rectangular and semi-elliptical slots

Figure 6 shows the model results in differential mode for the 3 rectangular slots (left-hand side) and the 3 semi-elliptical slots (right-hand side). The right-hand result in Figure 6 is in good agreement with the measured results shown in Figure 5.

Discussion: If you consider a defect in a material as to be like a time series as shown in black in Figure 7 and the cross-section of the fields generated by the coil as another signal, shown in blue, then the eddy-current signal, shown in red, can be thought of as the convolution of these signals. The series shown on the left-hand side of the Figure are those you would typically see with a standard pancake coil. The fields are, in cross-section, bipolar, so the convolved signal is very spread out and complicated. The signals on the right-hand side are those we see with the fields from the tangential coils in the weld scan probe. The field profile is much more focused and is not bipolar. Therefore the convolved signal is not smeared out by the coil geometry and is much simpler and hence more focused. It makes defect discrimination and sizing much easier.

Without noise, the convolved signal can be deconvolved to give the defect signal if the field signal is known. Noise is always an issue with eddy-current inspection and the complex bipolar shaped fields from pancake coils usually makes deconvolution of eddy-current signals impractical; however, the simpler and more focused nature of tangential coil fields make this more attractive approach.

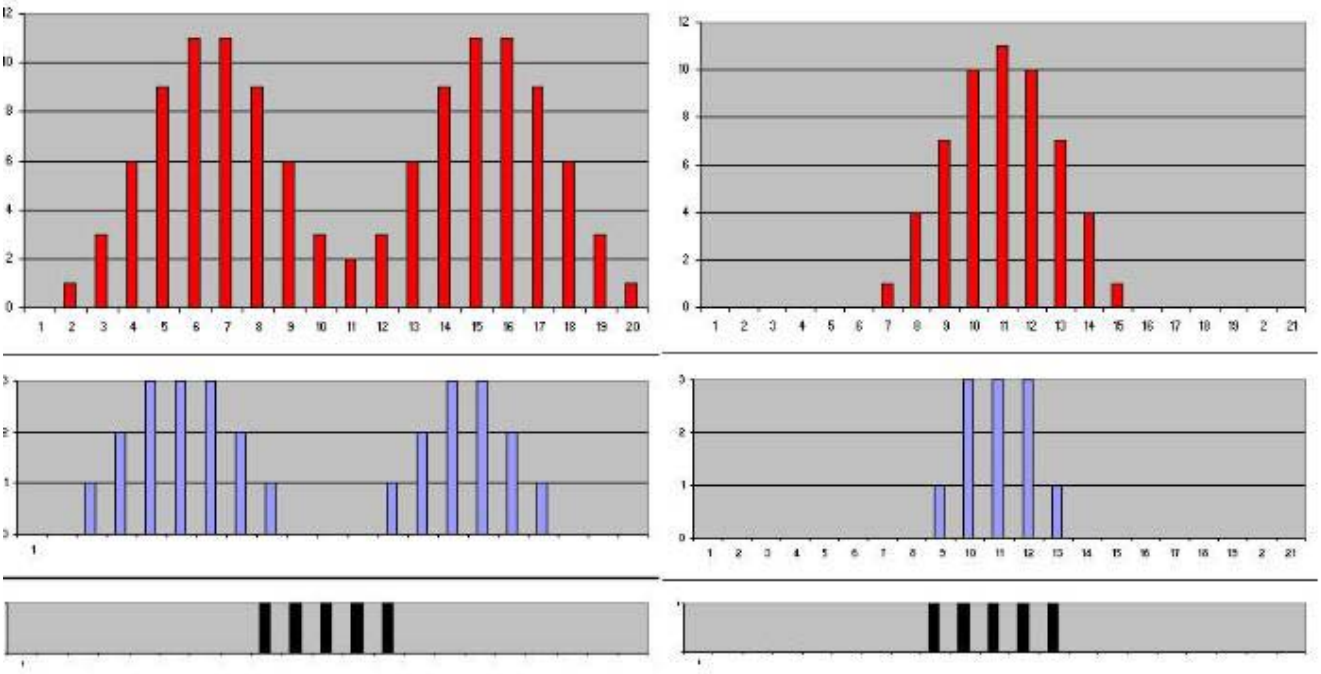

Figure 7 – defect, probe field (pancake and tangential) and eddy-current (convolved) signals

A simplistic approach to deconvolution, being simple is very easy to apply, can be seen by looking at the convolved signal shown in Figure 7. The defect ends occur when the convolved signal drops to approximately one third of the maximum value. This approach can be used with both the modeled and measured differential mode results and yields the results shown in the following table.

Actual length (mm)	Modeled results	Measured results
5	7	8
10	11	12
20	21	20

The left-hand side of Figure 8 shows the modeled signal from the 10 mm semi-elliptical slot, where the signal above one third of the max has been changed to unity, otherwise zero. The same approach has been done on the signal from the measured signal from the 20 mm semi-elliptical defect on the right-hand side of the Figure. Simply counting the ones in the columns determines the slot length.

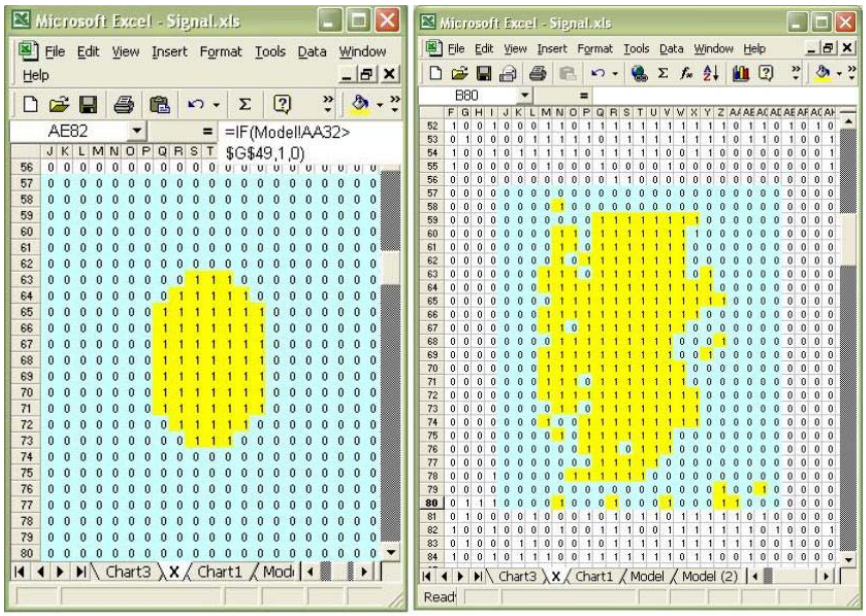

Figure 9 – 10 mm modeled semi-elliptical slot (left) and 20 mm measured semi-elliptical slot

The WeldScan probe is ideal for locating and sizing the defects at the surface for all the reasons already discussed; however, it comes at a cost: poor coupling with the work-piece. If you look again at the electric field shown in Figure 2, you can see the point of circulation of the fields on either side of the probe. This is the concentration point of the magnetic fields and as you can see it could be some distance from the defect and will be entering at an angle less than normal. Therefore, the penetration of the magnetic field and the circulation of eddy-currents will be near the surface. As the name of the probe implies, this probe is best suited for use with ferrous materials where the eddy-current regime is near-surface anyway. Depth information will be limited with this probe as the currents are encouraged to flow just beneath the surface. Indeed, modeling has shown that there is very little change in the signal for 20mm slots of depths of 1 – 2 mm. Defect depth information must come from information assumed from the material properties and assumptions about the defect geometry. The surface extent of the defect then implies the defect depth.

Conclusions: We have shown that proven eddy-current modeling techniques can be used to understand the behavior of the eddy-current tangential coils, WeldScan probes. We have seen that these probes give a much simpler excitation in the eddy-current regime and therefore can provide much more accurate defect sizing and location characteristics than conventional eddy-current probes. A simple masking approach has been shown to be effective in defect sizing and location. However, because of the poor coupling characteristics of the probe, depth information, except in the near surface regime, will have to be assumed a characteristic of the defect length.

References:

1. S. A. Jenkins, 'Analyst's Guide – Eddy current modelling', http://www.eddycentre.com/rcentre/aguide.pdf
2. J R Bowler, 'Eddy current calculations using half-space Green's functions', J. Appl. Phys, Vol 61, No 3, pp 833-839, February 1987.